A comparison of factors that led to the extreme sea ice minima in the 21st century in the Arctic Ocean

Xi Liang[1], Xichen Li[2], Haibo Bi[3, 4], Martin Losch[5],

Yongqi Gao[6], Fu Zhao[1], Zhongxiang Tian[1], Chengyan Liu[7]*

[1]*Key Laboratory of Marine Hazards Forecasting, National Marine Environmental Forecasting Center, Ministry of Natural Resources, Beijing, China*

[2]*International Center for Climate and Environment Sciences, Institute of Atmospheric Physics, Chinese Academy of Sciences, Beijing, China.*

[3]*Key laboratory of Marine Geology and Environment, Institute of Oceanology, Chinese Academy of Sciences, Qingdao, China*

[4]*Laboratory for Marine Geology, Qingdao National Laboratory for Marine Science and Technology, Qingdao, China*

[5]*Alfred-Wegener-Institut, Helmholtz Zentrum für Polar- und Meeresforschung, Bremerhaven, Germany*

[6]*Nansen Environmental and Remote Sensing Center/Bjerknes Center for Climate Research, Bergen, Norway*

[7]*Southern Marine Science and Engineering Guangdong Laboratory (Zhuhai), China*

Corresponding author: Chengyan Liu (liuchengyan@sml-zhuhai.cn)

Abstract

The extreme Arctic sea ice minima in the 21st century have been attributed to multiple factors, such as anomalous atmospheric circulation, excess solar radiation absorbed by open ocean, and thinning sea ice in a warming world. Most likely it is the combination of these factors that drive the extreme sea ice minima, but it has not been quantified, how the factors rank in setting the conditions for these events. To address this question, the sea ice budget of an Arctic regional sea ice-ocean model forced by atmospheric reanalysis data is analyzed to assess the development of the observed sea ice minima. Results show that the ice area difference in the years 2012, 2019, and 2007 is driven to over 60% by the difference in summertime sea ice area loss due to air-ocean heat flux over open water. Other contributions are small. For the years 2012 and 2020 the situation is different and more complex. The air-ice heat flux causes more sea ice area loss in summer 2020 than in 2012 due to warmer air temperatures, but this difference in sea ice area loss is compensated by reduced advective sea ice loss out of the Arctic Ocean mainly caused by the relaxation of the Arctic Dipole. The difference in open water area in early August leads to different air-ocean heat fluxes, which distinguishes the sea ice minima in 2012 and 2020. Further, sensitivity experiments indicate that both the atmospheric circulation associated with the Arctic Dipole and extreme storms are essential conditions for a new low record of sea ice extent.

1. Introduction

Over the past decades, the Arctic summertime sea ice thickness has declined substantially as documented in submarine and satellite records (Kwok and Rothrock, 2009; Kwok, 2018; Bi et al., 2018), and the shrinking and thinning of the Arctic sea ice has led to a transition from a multiyear ice-dominated Arctic towards a first-year ice-dominated Arctic due to Arctic amplification (Maslanik et al., 2011; Serreze and Barry 2011; Lindsay and Schweiger, 2015; Lang et al., 2017). This has had a significant impact on the lower latitude atmospheric circulation patterns (Cohen et al., 2014; Francis and Vavrus, 2015; Barnes and Polvani, 2015), for example, the sea ice loss is thought to induce increased summer precipitation in northern Europe (Screen et al. 2013). Drastic sea ice decline can also greatly affect the Arctic flora and fauna (Meier et al., 2014), native communities (Hovelsrud et al., 2008; Rasmussen, 2011), and remote Eurasian climate (Gao et al., 2015). According to the National Snow and Ice Data Center (NSIDC) Sea Ice Index (Fetterer et al., 2017), the Arctic sea ice extent was at the record minima during summers 2012, 2020, 2019, 2016, and 2007 in ascending order (Figure 1). Studying the mechanisms responsible for these extreme sea ice minima can improve our understanding of the overall processes driving seasonal sea ice loss and the potential implications of the historical sea ice record for future evolution.

Indeed, previous studies have already identified some dynamical (Serreze et al., 2003; Rigor and Wallace, 2004; L' Heureux et al., 2008; Wang et al., 2009; Woodgate et al., 2010; Lee et al., 2017; Ding et al., 2017) and thermodynamical (Lindsay and

Zhang, 2005; Perovich et al., 2008, 2011; Graversen et al., 2011; Flocco et al., 2012; Zhang et al., 2008, 2013) mechanisms responsible for the sea ice decline in the past decades. By the dynamical mechanisms, the Arctic Dipole (AD) atmospheric circulation, which is characterized by negative sea level pressure anomalies over the Siberian Arctic and positive sea level pressure anomalies over the Beaufort Sea-North America-Greenland (Wu et al., 2005), favored an enhanced mean meridional wind across the Arctic and directly gave rise to the sea ice loss (Wang et al., 2009) through mechanically pushing sea ice towards Fram Strait. The anomalous AD atmospheric circulation prevailed in every early summer from 2007 to 2012 (Ogi and Wallace, 2012; Overland et al., 2012) and thereby maintained the low sea ice extents. Thermodynamically, starting from low sea ice extent in the previous summer, the sea ice cover formed in the previous autumn and winter is dominated by first-year ice that is thin and vulnerable to changes in atmospheric and oceanic forcing and easy to melt in the following summer, primarily driven by the stronger ice-albedo feedback (Curry et al., 1995) in the presence of more open water (Kay et al., 2008; Jackson et al., 2010; Stroeve et al., 2012). Low sea ice extents were also further reduced by northward oceanic heat transport through the Bering Strait driven by the strong AD winds (Woodgate et al., 2010), accelerating the drastic thinning of sea ice (Steele et al., 2004; Shimada et al., 2006; Comiso and Hall, 2014; Kwok, 2018). In addition, the near-surface temperature maximum layer at a typical depth of 25-35 m also has the potential to induce sea ice basal melt (Jackson et al., 2010). In 2020, a warm air temperature anomaly also contributed to the record-low summer sea ice extent

(Ballinger et al., 2020).

According to observational data (NSIDC; Fetterer et al., 2017), the Arctic sea ice extent in 2012 reached the record-low of 2007 in the last week of August and set a new record minimum of 3.41×10^6 km^2 at the end of the melting season. The sea ice distribution in summer 2012 was affected by a strong storm, 'the Great Arctic Cyclone of August 2012' (Simmonds and Rudeva, 2012). To quantify the impact of this cyclone on the 2012 record-low Arctic sea ice extent, Zhang et al. (2013) employed a coupled ice-ocean model and found an intense sea ice bottom melt caused by increased upward ocean heat transport when the storm passed in early August 2012. However, Zhang et al. (2013) also suggested that it would have been possible to simulate a record-low summer sea ice minimum in 2012 even without the storm, implying that the atmospheric AD pattern may have been more important than the storm. In summer 2016, six distinct cyclones impacted the Arctic Ocean between 10 August and 10 September (Yamagami et al., 2017), and some of them had comparable sizes and intensity but longer persistence compared to the 'the Great Arctic Cyclone of August 2012'. However, the record-low sea ice extent in summer 2016 was still not as extreme as that in 2012. The AD time series in melting seasons between 2000 and 2020 derived from the Japanese 55-year Reanalysis (JRA55; Kobayashi et al., 2015; Harada et al., 2016) data shows that the strength of the AD greatly reduces in summer 2016 compared to that in summer 2012 (Figure 2), further indicating that a new low sea ice extent record is unlikely without favorable AD conditions.

So far, multiple factors are thought to set the five record-low sea ice minima in the 21st century, yet their relative importance and differences have not been quantitatively clarified. Furthermore, why wasn't there any new record-low sea ice extent between 2013 and 2020? In this study, we employ a coupled Arctic regional sea ice-ocean model and conduct sensitivity experiments with a quantitative sea ice budget analysis, to clarify the relative roles of the dynamical and thermodynamical factors leading to the different sea ice minima in the 21st century. This paper is organized as follows. Section 2 describes the model and experiment design. Evaluation of the model performance with respect to sea ice is shown in section 3. The sea ice budget analysis for the five sea ice minima is given in section 4. Section 5 presents the result of the sensitivity runs. Discussion and conclusion are presented in section 6.

2. Model and Experiment Description

The coupled Arctic regional sea ice-ocean model used in this study is based on the Massachusetts Institute of Technology general circulation model (MITgcm, Marshall et al., 1997; https://mitgcm.org), with a horizontal resolution of ~18 km (Losch et al., 2010; Liang et al., 2019). There are 420 × 384 horizontal grid points and 50 vertical ocean layers, with intervals ranging from 10 m at the sea surface to 456 m at the bottom. The MITgcm contains a zero-layer thermodynamic-dynamic sea ice model (Losch et al., 2010). This model includes a prescribed sub-grid Ice Thickness Distribution (ITD) with 7 thickness categories following Hibler (1984). Sea ice ridging in convergent motion only changes net ice volume, but not the ice thickness distribution (Castro-Morales et al., 2014). The prescribed ITD allows ice to form even when the mean ice thickness is large and thus reduces a low thickness bias. Due to the lack of thermal inertia, the zero-layer thermodynamics are known to overestimate the seasonal variations. The monthly open boundary conditions are derived from the Estimating the Circulation and Climate of the Ocean phase Ⅱ: high resolution global ocean and sea ice data synthesis (Menemenlis et al., 2008). Details of the parameterization settings can be found in Liang and Losch (2018).

Initialized from climatological hydrography fields derived from the World Ocean Atlas 2005 (WOA05; Locarnini et al., 2006), the model is integrated repeatedly for 20 model years driven by the climatological annual cycle atmospheric forcing data with 3-hourly temporal resolution. The climatological atmospheric forcing data, denoted by Atmospheric Forcing Climatological State (AFCS), are derived from the average values of the JRA55 data between 1979 and 2013. The last days in leap years in the JRA55 data are simply excluded. The sea ice and ocean states on the last day of the 20 model years are saved as restart files, denoted by Restart File Climatological State (RFCS), for one baseline experiment (Table 1). Initialized from the RFCS, the baseline run, denoted by CTRLRUN, is driven by 3-hourly JRA55 data from 1980 to 2020. The modeled sea ice and ocean states are saved as daily averages. The sea ice and ocean states on 1 May 2007, 1 May 2012, and 1 May 2020 are denoted by RF07 (Restart File on 1 May 2007), RF12 (Restart File on 1 May 2012), and RF20 (Restart File on 1 May 2020), respectively. These three restart files are used in eight sensitivity runs SENSR01 to SENSR08. As there is a strong spring sea ice barrier (Bushuk et al., 2020), and summer sea ice extent directly links to sea ice state at the onset of melting season, our sensitivity runs are initialized from the different model states on 1 May. Each sensitivity run integrates for 5 months forced by a different atmospheric state. The detailed setting of the eight sensitivity runs is listed in Table 1. In general, they are designed to assess the relative importance of preconditioning sea ice state at the onset of the melting season and atmospheric condition in the melting season on the sea ice minima. Here, the atmospheric conditions from JRA55 are further classified into three typical states based on the strength of the AD (Figure 2): 1) the atmospheric state from 1 May 2020 to 1 October 2020 represents the normal atmospheric condition, i. e. the AD is very weak. 2) the atmospheric state from 1 May 2007 to 1 October 2007 represents the extremely strong AD atmospheric condition. 3) the atmospheric state from 1 May 2012 to 1 October 2012 represents the normal AD atmospheric condition but with an extreme storm. Detailed information of inter-comparison among the eight sensitivity runs is presented in Section 5. For all sensitivity runs, daily model states are saved.

3. Sea Ice Evaluation of the Baseline Experiment

Since the atmospheric forcing data is changed from climatological fields to real-time fields, the basin mean upper 200 m ocean temperature of the CTRLRUN run reaches a quasi-equilibrium state after about 5-years of model adjustment (Figure 3a). The basin averaged sea ice concentration does not show any obvious adjustment features (Figure 3b) to the transient response to the atmospheric and oceanic forcing.

Since this study focuses on the sea ice evolution and the corresponding oceanic upper layer, we conclude that the model states after the adjustment period can be used in the analysis.

To give a brief evaluation of the modeled sea ice in the CTRLRUN run, we compare the simulated sea ice extent and thickness with the satellite observations (Figure 4). The modeled sea ice extent evolution from 2002 to 2020 is compared to the daily observations derived from medium resolution passive microwave sea ice concentration data of the Advanced Microwave Scanning Radiometer series (AMSR-Earth Observing System and AMSR2; Pedersen et al., 2017). The AMSR sea ice concentration observations from June 2002 to May 2017 are processed under the umbrella of the European Space Agency-Climate Change Initiative (ESA-CCI; Meier et al., 2013) project. Due to the data gap between the service period of the AMSR-E and that of the AMSR2 after 2012, the sea ice concentration observations from October 2011 to July 2012 are unavailable. The AMSR sea ice concentration observations after May 2017 are processed by the University of Bremen using the ARTIST Sea Ice (ASI; Spreen et al., 2008) algorithm. The sea ice extent evolution in the CTRLRUN run agrees well with the satellite data. Moreover, the CTRLRUN run properly captures the five sea ice extent minima in the 21st century (Figure 4a), and the simulated values are largely consistent with the observations in summer 2007, 2012, 2019, and 2020. However, our model simulated sea ice extent in summer 2016 that is 0.8×10^6 km^2 smaller than observed. The observed record-low sea ice extent in ascending order happened in 2012, 2020, 2019, 2016, and 2007. In the CTRLRUN

run, the modeled record-low sea ice extent in ascending order happens in 2012, 2016, 2020, 2019, and 2007. We note that our model simulates a systematic lower sea ice extent in wintertime probably due to the modeled sea surface temperature bias in low latitudes in the model domain.

The modeled monthly mean sea ice thickness evolution in the cold season from 2002 to 2020 is evaluated against the observation derived from Envisat and Cryosat-2 data. Here, the cold season includes the months from October to April of the next year. The observed sea ice thickness before May 2011 is provided by the Radar Altimeter-2 instrument on the Envisat satellite (Hendricks et al., 2018) and processed in the ESA-CCI project. The observed sea ice thickness after September 2011 is provided by the Synthetic Aperture Interferometer Radar Altimeter instrument on the Cryosat-2 satellite (Hendricks et al., 2018), in which the data before May 2017 are processed in the ESA-CCI project while the data after September 2017 are processed in the Alfred-Wegener-Institut (AWI) Sea Ice Radar ALtimetry (SIRAL) project. In general, the sea ice in CTRLRUN run is thinner than the observation, and the bias after 2007 is larger at the beginning of the freezing season than at the end of the freezing season (Figure 4b). Note that the observations are only available in some regions of the ice zone, thus no result relating to trends in sea ice thickness evolution can be derived from the comparison. Considering that the satellite observed sea ice thickness from radar altimetric instruments do have relatively large uncertainties (Ricker et al., 2014), the modeled sea ice thickness evolution may be still in a plausible range.

To further assess our model, we compare the spatial distribution of the modeled sea ice concentration with the AMSR observations on 24 September of the five years with record-low sea ice extent (Figure 5). The modeled sea ice distribution in 2007, 2019, and 2020 in the CTRLRUN run is generally similar to the observations, yet the modeled sea ice distribution in 2012 has an unrealistic sea ice tongue appearing over the Mendeleyev Ridge (Figure 5a). The modeled sea ice extent bias in 2016 arises from the excessive melting in the Pacific sector of the Arctic (Figure 5g). In general, the simulated sea ice concentration is lower than in the observations. It is also worth noting that the sea ice concentration derived by the ASI algorithm (Figure 5e, 5f) shows systematically higher value compared to that of the ESA-CCI project, in part because the former is a near-real-time product while the latter is a reanalyzed product.

4. Sea Ice Budget Analysis of the Baseline Experiment

Although sea ice extent is used very often to quantify the change in Arctic sea ice cover, it does not allow a consistent budget analysis. If ordered by increasing size, the order of sea ice ice extent minima in the five summers is not the same as the order of sea ice area minima or sea ice volume minima. According to reanalysis data of the Pan-Arctic Ice Ocean Modeling and Assimilation System (PIOMAS; Zhang and Rothrock, 2003), the sea ice volume minimum in 2019 is lower than in 2012 and the year 2016 is not among the five lowest. Also, sea ice area minimum in 2019 is the 5th lowest and 2007 is the 3rd lowest, which is different from the order of sea ice extent minima. Since sea ice extent is more closely related to sea ice area than sea ice volume, we focus on analyzing the sea ice area budget. The sea ice volume budget is included as a complementary analysis.

The sea ice model in the MITgcm is a viscous-plastic dynamic and zero-layer thermodynamic model (Hibler, 1979, 1980; Zhang and Hibler, 1997). The so-called zero-layer thermodynamics assumes one layer of ice underneath one layer of snow. Neither snow nor ice have a heat capacity so that the vertical temperature gradient through the ice is constant. The snow layer affects sea ice thermodynamics by modifying the ice surface albedo and effective heat conductive coefficient. The snow can be flooded when enough snow accumulates on top of the ice and its weight submerges the ice. The sea ice model divides each grid area into two parts: the open water area and the ice-covered area. The fraction of the ice-covered area in the grid cell is sea ice concentration (*C*). In each bin, the sea ice rate of change is determined by the atmospheric heat flux on the ice surface, the oceanic heat flux on the ice bottom, the atmospheric heat flux on the sea surface in the open water area, the sea ice advection, and the sea ice deformation. Sea ice deformation can lead to ridge formation. In our model, the ridging processes are parameterized by simply capping sea ice concentration at 100% (Schulkes, 1995). To quantitatively diagnose the contribution of each term, we define a control region covering the Arctic basin (Figure 6). In the control region with area *S*, the change of sea ice area (ΔA) and volume (ΔV) over the time interval (Δt) can be expressed as:

$$\Delta A = \langle \omega_{io} \rangle + \langle \omega_{ai} \rangle + \langle \omega_{ao} \rangle + \left\langle \frac{\partial \psi_{advx}}{\partial x} + \frac{\partial \psi_{advy}}{\partial y} \right\rangle + \langle \omega_{ridging} \rangle \quad (1)$$

$$\Delta V = \langle \theta_{io} \rangle + \langle \theta_{ai} \rangle + \langle \theta_{ao} \rangle + \langle \theta_{fl} \rangle + \left\langle \frac{\partial \varphi_{advx}}{\partial x} + \frac{\partial \varphi_{advy}}{\partial y} \right\rangle \quad (2)$$

where the variables (x, y) represent the two orthogonal axes in the model domain. The operator $<>$ represents the integral over area S and time Δt, that is, $<*>=\Delta t\iint * dS$. $dS=dxdy$ is the area element of the integration. ω_{io}, ω_{ai}, and ω_{ao} are the rates of change of sea ice concentration induced by the oceanic heat flux at the ice bottom, the atmospheric heat flux at the ice surface, and the atmospheric heat flux at the sea surface in the open water area, respectively. θ_{io}, θ_{ai}, θ_{ao}, and θ_{fl} are the rates of change of grid-mean sea ice thickness due to the oceanic heat flux at the ice bottom, the atmospheric heat flux at the ice surface, the atmospheric heat flux at the sea surface in the open water area, and the snow flooding term, respectively. (ψ_{advx}, ψ_{advy}) and (φ_{advx}, φ_{advy}) are the components of advection of sea ice concentration (C) and grid-mean sea ice thickness (H). $<\partial\psi_{advx}/\partial x+\partial\psi_{advy}/\partial y>$ and $<\partial\varphi_{advx}/\partial x+\partial\varphi_{advy}/\partial y>$ represent the net sea ice area and volume fluxes advected across the control region boundaries. In our simulations, the model outputs the ocean and sea ice states daily, so that Δt = 86400 s. Variables (ω_{io}, ω_{ai}, ω_{ao}, θ_{io}, θ_{ai}, θ_{ao}, θ_{fl}, ψ_{advx}, ψ_{advy}, φ_{advx}, φ_{advy}) are directly saved by the model and $<\omega_{ridging}>$ is calculated as the residual term. $<\omega_{ridging}>$ mainly consists of the change of area by ridging processes. Sea ice ridging does not change the integrated ice volume, because it is only a volume redistribution, but the associated convergence does change the ice volume within the control region as ice can be moved across the boundaries. As this flux of ice volume over the boundaries is quite small compared to other terms, we ignore the sea ice volume change due to sea ice ridging in Eqs. 2.

The growth-decay evolution of the sea ice area and volume in the control region during 2006-2007, 2011-2012, 2015-2016, 2018-2019, and 2019-2020 are shown in Figure 7. For the onset sea ice conditions during the periods of interest, the sea ice area and volume are largest in September 2006 and lowest in September 2019. The sea ice condition in September 2011 is quite close to that in September 2018 in terms of area and volume. During the sea ice growth season, new ice continuously forms in open water area and so that the control region is fully covered by sea ice around 25 December during the five periods of interest. However, the sea ice volume around 25 December still shows significant divergence, with a minimum in 2019 and a maximum in 2006. Sea ice volume in the control region stops growing around 10 May. From May to September, the modeled largest sea ice area reduction during the five periods of interest is 5.62×10^6 km^2 in 2016, followed by 5.54×10^6 km^2 in 2012, 5.42×10^6 km^2 in 2020, 5.14×10^6 km^2 in 2019, and 4.59×10^6 km^2 in 2007. Although the modeled largest sea ice area reduction in summer 2016 exceeds the value in summer 2012, the modeled record-low sea ice extent in summer 2012 is still lower than that in summer 2016. From May to September, the modeled largest sea ice volume reduction in summer 2007, 2012, 2016, 2019, and 2020 are 11.99×10^3 km^3, 13.68×10^3 km^3, 13.96×10^3 km^3, 13.14×10^3 km^3, and 13.37×10^3 km^3, respectively.

For the following discussion, the daily sea ice increments in the control region are broken down into their constituents (Eqs. 1 and 2) for a full growth-decay cycle during 2011-2012 (Figure 8). In the freezing season, the increase in sea ice area is dominated by the heat flux between the atmosphere and sea surface in the open water area $<\omega_{ao}>$ term (magenta line in Figure 8a), implying that new ice continuously freezes when cold air blows over the relatively warm sea surface. The sea ice area growth due to atmosphere-ice heat flux $<\omega_{ai}>$ is nearly zero in the freezing season (green line in Figure 8a), meaning that the heat loss from the ice to the atmosphere leads to the increase in the ice thickness. The heat flux between ice bottom and ocean $<\omega_{io}>$ term (blue line in Figure 8a) is a loss term to the sea ice area in all seasons. The $<\partial\psi_{advx}/\partial x+\partial\psi_{advy}/\partial y>$ term closely relates to the sea ice drift and the definition of the control domain. In the freezing season, the $<\partial\psi_{advx}/\partial x+\partial\psi_{advy}/\partial y>$ term alternately shows net sea ice area input or output of the control region. In the melting season, the $<\partial\psi_{advx}/\partial x+\partial\psi_{advy}/\partial y>$ term tends to reduce the sea ice area due to the Transpolar Drift-induced sea ice advection toward Fram Strait (red line in Figure 8a). Furthermore, the $<\partial\psi_{advx}/\partial x+\partial\psi_{advy}/\partial y>$ term shows relatively larger amplitude in wintertime than summertime, probably resulting from the advection of high sea ice concentration in wintertime. It is worth noting that the sea ice area lost through the ridging $<\omega_{ridging}>$ term (cyan line in Figure 8a) is comparable to that by the $<\omega_{io}>$ term, indicating that sea ice ridging also plays an important role in the sea ice area reduction. In the melting season, the decrease of sea ice area is governed by the $<\omega_{ai}>$, $<\omega_{ao}>$, and $<\omega_{ridging}>$ terms. The $<\omega_{ai}>$ term can induce direct sea ice area loss from May to August when the sea ice in some grid cells are thin enough and the warm air can directly result melting the thin ice completely. The $<\omega_{ao}>$ term also creates a large reduction in the sea ice area by decreasing grid-cell averaged sea ice thickness. After sea ice has melted locally, the remaining heat warms the ocean, and then lateral processes such as advection or horizontal diffusion in the ocean can move this heat underneath the ice in the neighboring grid cells where it can lead to more melting. In the Hibler model, the air-ocean heat flux is used to melt the thick sea ice laterally until there is no more ice in the grid cell. This is based on the assumption that the heat in the ocean is immediately distributed within the grid cell and that the grid cell remains at the freezing temperature as long as there is some ice. Only if there is heat left after all ice is melted, the ocean is actually warmed by the air-ocean heat flux.

In all seasons, the sea ice volume change is mainly dominated by the atmosphere-ice heat flux $<\theta_{ai}>$ (green line in Figure 8b) and the heat flux between the atmosphere and sea surface in the open water area $<\theta_{ao}>$ (magenta line in Figure 8b) terms. The $<\theta_{ai}>$ and $<\theta_{ao}>$ terms create comparable sea ice volume increments from September to October. Along with new ice continuously forming in the freezing season, the fraction of totally ice-covered area in the control region also increases, so that the $<\theta_{ai}>$ term is obviously larger than the $<\theta_{ao}>$ term from November to May. During the period from June to September, the large sea ice volume loss is primarily caused by the $<\theta_{ai}>$ term. Thereafter, the $<\theta_{ao}>$ term starts to result in sea ice volume loss in the expanding open water area. Like $<\omega_{io}>$, $<\theta_{io}>$ (blue line in Figure 8b) also acts to reduce the sea ice volume in all seasons. The $<\omega_{io}>$ and $<\theta_{io}>$ terms peak in late autumn and early winter, because during this period the sea ice growth rate stays at a high level leaving dense (saline) surface water behind. The dense surface water leads to increased vertical convection and upward oceanic turbulent heat flux yielding more basal ice melt. Note that the enhanced sea ice area and volume losses during

6-10 August are caused by the 'the Great Arctic Cyclone of August 2012', which enhanced the sea ice basal and surface melting by the drastic wind-driven upper ocean mixing and heat fluxes from warm air to open water surface. The changes in ice volume due to the $\langle \theta_{fl} \rangle$ and $\langle \partial\varphi_{advx}/\partial x+\partial\varphi_{advy}/\partial y \rangle$ terms are small compared to the thermodynamical terms.

To determine the contributions to the record-low sea ice extent minima, we calculated the accumulated sea ice area increments from 1 May in the five summers (Figure 9). As a first observation, the accumulated sea ice area loss due to $\langle \omega_{ao} \rangle$ determines the record-low sea ice extent in summer 2007, 2012, and 2019 (red, green, cyan lines in Figure 9d). The relatively large sea ice thickness as presented in sea ice volume evolution (Figure 7b) in May 2007 sets the initial conditions so that the record-low sea ice extent in 2007 is still substantially highest in these five years. The sea ice area in the middle of July in 2007 is significantly higher than that in 2012 by approximately 0.5×10^6 km^2 (red, cyan lines in Figure 9a), and thus less solar radiation enters into the ocean through open water area in ice zone in the rest of the melting season of 2007. As a consequence, the record-low sea ice extent in summer 2007 is substantially higher than the other years. The sea ice area difference between summer 2019 and summer 2012 amplified around 10 August (red, green lines in Figure 9a), thereafter solar radiation entering into the ocean through open water areas in the ice zone contributes to the record-low sea ice extent in these two years, while the accumulated sea ice area losses due to the $\langle \omega_{ai} \rangle$ and $\langle \partial\psi_{advx}/\partial x+\partial\psi_{advy}/\partial y \rangle$ terms before 10 August in these two years are almost the same (red, green lines in Figure 9c, 9e).

Between summer 2012 and summer 2020, large differences exist in the accumulated sea ice area loss due to the $<\omega_{ai}>$ and $<\partial\psi_{advx}/\partial x+\partial\psi_{advy}/\partial y>$ terms (red, blue lines in Figure 9c, 9e), and a moderate difference exists in the accumulated sea ice area loss due to the $<\omega_{ao}>$ term (red, blue lines in Figure 9d). Figure 7b shows sea ice volume in the control region on 1 May 2020 is lower than that on 1 May 2012, indicating that the basin-scale Arctic sea ice on 1 May 2020 is thinner than that on 1 May 2012. The relatively thinner ice is easy to melt entirely, especially under anomalous warm air condition in summer 2020. Thus the atmosphere-ice surface heat flux generates more sea ice area loss by directly melting the thin ice at the ice surface in summer 2020 than that in summer 2012. This part of difference of sea ice area loss due to ice surface melting is compensated by the enhanced sea ice advection out of the control region in summer 2012, mainly due to the strengthened Transpolar Drift driven by atmospheric circulation. Along with the different expanding speeds of open water area in summer 2012 and 2020, more solar radiation enters the ice zone through open water area in summer 2012 and enhances the sea ice area loss.

Figure 9b shows that the strongest accumulated sea ice area loss due to the $<\omega_{io}>$ term occurs in summer 2016 and followed by that in summer 2012 (black and red lines in Figure 9b). Figure 7b indicates that the basin-scale Arctic sea ice on 1 May 2012/2016 is thicker than that on 1 May 2019/2020. Compared to 2019 and 2020, the relatively thicker ice in summer 2012 and summer 2016 should take longer to melt, and slow down the expanding open water area. However, the accumulated sea ice area losses due to the $<\omega_{ao}>$ term in summer 2012 and summer 2016 are also relatively large (black and red lines in Figure 9d). This can be attributed to six distinct cyclones impacting the western Arctic Ocean between 10 August and 10 September 2016 (Yamagami et al., 2017). At least one of the cyclones was comparable in size and intensity to ‘the Great Arctic Cyclone of August 2012’, but was more persistent. The activities of the cyclones strongly perturb the sea ice and upper ocean and lead to sea ice deformation and ocean mixing, further inducing enhanced sea ice basal melting. Although basin-scale sea ice thickness in summer 2019 is close to that in summer 2020 (Figure 7b), the accumulated sea ice area loss due to the $<\omega_{ai}>$ term at the end of summer 2020 is largely higher than that at the end of summer 2019 (blue and green lines in Figure 9c). This results partly from the significantly higher air temperature in summer 2020 than in previous years (Ballinger et al., 2020), which increases ice surface melting by intensified sensible heat flux from air to ice surface. The accumulated sea ice area loss due to $<\partial\psi_{advx}/\partial x+\partial\psi_{advy}/\partial y>$ term shows intermittently decreasing signals with small values in 2020 and large values in 2007 and 2012 (Figure 9e), probably originating from the relaxation of the AD after 2012. The accumulated sea ice area loss due to the $<\omega_{ridging}>$ term in summer 2007 is very different from the other four summers (Figure 9f).

Integrated from the beginnings of the five periods, the largest accumulated sea ice volume gain until 1 May occurs in 2019-2020 while the smallest gain occurs in 2006-2007, and their difference reaches approximately 2.9×10^3 km^3 (blue and cyan bars of the $\Sigma(\Delta V)$ term in Figure 10a). It implies a negative feedback commonly referred to the ice thickness-ice growth feedback (Notz and Bitz, 2017), that is, thinner ice in later autumn supports larger conductive heat fluxes through the ice-air interface in the following winter and spring, and eventually leads to larger ice-growth rates (blue and cyan bars of the $\Sigma(<\theta_{ai}>)$ term in Figure 10a). During the five periods of interest, the accumulated sea ice volume loss until 1 September due to sea ice basal melt ranges from 2.9×10^3 km^3 in 2006-2007 to 3.4×10^3 km^3 in 2015-2016 (the $\Sigma(<\theta_{io}>)$ term in Figure 10b). The accumulated sea ice volume loss until 1 September due to the sea ice advection term is large in 2006-2007 and 2018-2019, and small in 2011-2012 (the $\Sigma(<\partial\varphi_{advx}/\partial x+\partial\varphi_{advy}/\partial y>)$ term in Figure 10b).

5. The Absence of A New Record-Low Sea Ice Extent Post-2012

The shrinking and thinning of the Arctic sea ice in the past decades preconditioned the 2007 sea ice extent minimum (Kwok, 2007; Lindsay et al., 2009). The persistent atmospheric AD pattern in every early summer from 2007 to 2012 (Ogi and Wallace, 2012; Overland et al., 2012) contributes to the record-low sea ice extents in 2007 and 2012, and to the summertime low sea ice extents between these two years. The Arctic sea ice in May continuously thins from 2012 to 2020 (Figure 7b). Why does this thinning not lead to new record-low sea ice extents after 2012?

In our sensitivity runs, a comparison between the SENSR01, SENSR02 runs, and the model states in summer 2012 in the CTRLRUN run (blue, green, and black lines in Figure 11) implies the importance of preconditioning sea ice state at the onset of the melting season on sea ice minima under normal AD atmospheric condition with an extreme storm. The RF07, RF12, RF20 represent three sea ice conditions: heavy ice state, moderate ice state, mild ice state (Figure 7b, Table 1). The result shows that a new record-low sea ice extent will occur if the normal AD in conjunction with an extreme storm reemerges with a mild ice state at the onset of melting season in the previous 2 years.

The differences between the SENSR03 and SENSR04 runs (purple and orange lines in Figure 11) indicate the importance of preconditioning sea ice state at the onset of melting season on sea ice minima under extremely strong AD atmospheric conditions. The result shows that without extreme storms, the extremely strong AD summertime atmospheric conditions do not create a new record-low sea ice extent independent of the sea ice state being moderate or mild at the onset of the melting season.

The differences between the SENSR03, SENSR05, SENSR06 runs, and the CTRLRUN run in summer 2012 (purple, red, brown, and black lines in Figure 11) underline the importance of summertime atmospheric conditions, as well the relative influences of an extreme storm, for sea ice minima under moderate sea ice condition. The result shows that with a moderate ice state at the onset of the melting season, the normal AD in conjunction with an extreme storm has the greatest potential of inducing sea ice minima, followed by the extremely strong AD condition, and the normal condition (black, purple, and red lines in Figure 11). Furthermore, the extreme storm contributes greatly to the record-low sea ice extent in 2012: the storm-induced sea ice extent reduction is close to 0.26×10^6 km^2 (brown and black lines in Figure

11).

Finally, comparing the SENSR07 run and the CTRLRUN run in summer 2012 (pink and black lines in Figure 11) shows that even though there is an extreme storm analogous to 'the Great Arctic Cyclone of August 2012' in summer 2020, the minimum sea ice extent in 2020 is not lower than the record-low sea ice extent in 2012. The differences between the SENSR02, SENSR08 runs and the CTRLRUN run in summer 2012 (green, gray, and black lines in Figure 11) show that without extreme storms, the normal AD summertime atmospheric condition will not lead to a new record-low sea ice extent with a mild ice state at the onset of the melting season. These results indicate that both the AD atmospheric circulation and extreme storms are essential conditions for a new record-low sea ice extent in recent years.

6. Discussion and Conclusion

Based on a sea ice budget analysis of a coupled Arctic sea ice-ocean model simulation, the contributions of the main drivers to the extreme sea ice minima in the 21st century are assessed quantitatively. These drivers include atmospheric heat fluxes over ice and ocean, heat flux between ice and ocean, sea ice export out of the Arctic Ocean, and sea ice ridging. Our results show that the dominant driver, which directly determines the difference in the record-low sea ice areas among 2012, 2019, and 2007, is the difference in the summertime sea ice area loss due to the air-ocean heat flux in open water fraction, while the contributions from other factors are small. The relatively thicker sea ice in May 2007 leads to the relatively later occurrence of open water area in the Arctic Ocean and thus less solar radiation absorbed by the open water area in the ice zone in the remaining melting period. The thick ice condition at the onset of the melting season in 2007 preconditions that the record-low sea ice extent in 2007 can be easily broken by a new low record along with the continuous trend of sea ice decline. The difference of the open water area in the ice zone between summer 2012 and summer 2019 increases after 10 August, thereafter the air-ocean heat fluxes induce different sea ice area losses in the two rest melting periods. The main drivers determining the difference of the record-low sea ice areas between 2012 and 2020 are more complicated. Compared with summer 2012, the air-ice heat flux generates more sea ice area loss in summer 2020 due to warmer air temperature (Ballinger et al., 2020), however, this part of increased sea ice area loss is compensated by the smaller sea ice area loss due to sea ice advection out of the Arctic Ocean, which is caused by the relaxation of Transpolar Drift driven by atmospheric circulation. Along with the different expansion rates of open water area in the ice zone, the difference in the air-ocean heat fluxes between summer 2012 and summer 2020 contributes to the two sea ice minima.

A question arises that why the summertime sea ice extent after 2012 does not create a new low record. Olonscheck et al. (2019) proposed that the Arctic sea ice variability is primarily governed by atmospheric temperature, and suggested that the observed record lows in Arctic sea ice area are a direct response to an warm atmosphere. Lukovich et al. (2021) suggested that the differences in the location and timing of extreme summertime storms in 2012 and 2016 determine their relative contributions to the two sea ice extent minima. 'The Great Arctic Cyclone of August 2012' is also found to be important for reaching the historical record-low sea ice extent in the satellite era. Based on our sensitivity experiments, we find that both the AD atmospheric circulation and extreme storms are essential conditions for a new low record of sea ice extent in recent two years. The atmospheric condition in the summers after 2012 does not lead to a lower sea ice extent record than that in summer 2012, because the extreme storm activity is low or the Arctic Dipole is weak. Note that the conclusions derived from the comparison of the sensitivity runs are plausible. For example, the storm activities in summer 2016 induce more sea ice area loss than that by the storm activities in summer 2012, if the storm activities in summer 2016 reemerges in summer 2020, a new low sea ice extent may break the 2012 record despite the reduced Arctic Dipole atmospheric circulation. Along with the likely continuous sea ice thinning in the future, a new low sea ice extent record seems to be easily possible if the Arctic Dipole strengthens again along with an extreme storm.

Experimental design and imperfect model physics may lead to biases. For example, replacing atmospheric data for Aug 1-15, 2012 by the 2007-2012 mean state could be improved, and there is a systematic bias between the modeled sea ice distribution and the observations, in both sea ice thickness and wintertime extent. Some of the model biases, for example in sea ice extent, can be attributed to atmospheric and oceanic forcing. Persistent biases in thickness are also a result of model physics. In our comparison with satellite data, the model consistently underestimates ice thickness probably because there is too little ice to start with after too much summertime melting. In almost all cases, however, the ice thickness falls within the estimated errors of the satellited data and the seasonal cycle matches the observations.

The simulated summer sea ice extent is generally consistent with the AMSR data with a tendency to underestimate the sea ice concentration (Figure 5). In 2012 and 2016, this ice area underestimation is stronger leading to too low ice extent and spurious features such as an ice tongue in 2012 and disjunct areas of sea ice in 2016. The overly strong melting in 2012 and 2016 may be attributed to the use of a zero-layer thermodynamic model without heat capacity. This model is known to exaggerate the seasonal cycle of ice thickness and to lead to a too early onset of melting (Semtner, 1976; Losch et al., 2010). Strong meteorological events are likely to amplify this effect. This implies a connection between strong winds and too much melting, for example, when strong winds increase the turbulent heat fluxes. Once the ice is too thin, the ice strength is too low leading to additional deformation, which in convergence may reduce the ice extent even further. The general underestimation of sea ice concentration in the model will exaggerate the kinematic response of the sea ice to wind forcing, potentially amplify the sea ice loss due to ridging process. The negative ice thickness bias at the onset of melting season results in open water probably appearing earlier in summertime in the model than in observations. This may amplify the contribution of the air-ocean heat flux in sea ice area loss.

Our conclusions are drawn from differences between experiments so that the effect of the model bias is reduced. Still, the problem is nonlinear and a thin ice bias may exaggerate some effects. Keeping this in mind, our conclusions may provide some insight into the future sea ice evolution. Keen et al. (2021) pointed out that there is probably a lack of diversity in implemented sea ice model physics, at least in most of the CMIP6 models. If more sophisticated sea ice model physics and a larger range of different model physics were available this could enhance our confidence in predicting Arctic sea ice extreme event. Meanwhile it is worth noting that the Arctic sea ice is an element in global climate system, and its evolution is intimately linked to the tropics and mid-latitudes (Tietsche et al., 2011; Winton, 2011; Swart et al., 2015; Baxter et al., 2019; Wang et al., 2020; Bi et al., 2021). Predicting the Arctic sea ice extreme event also relies on numerical models being able to simulate large climate variability on local and large scales.

Acknowledgments. This work is supported by the National Key R&D Program of China (2017YFE0111700, 2016YFC1402700, 2019YFE0105700). The authors thank the Japan Meteorological Agency for providing the JRA55 data (http://jra.kishou.go.jp/JRA-55/), the National Snow and Ice Data Center for providing the passive microwave sea ice concentration climate data record (https://nsidc.org/data/G02202/versions/2), the University of Bremen for providing the AMSR2 near-real-time sea ice concentration data (https://seaice.uni-bremen.de/data/amsr2/asi_daygrid_swath/n6250/), the Alfred-Wegener-Institut for providing the CryoSat-2 sea ice thickness data (https://data.meereisportal.de/data/cryosat2/version2.3/), and the Centre for Environmental Data Analysis of the United Kingdom for providing the AMSR series sea ice concentration reanalysis data, the Envisat and the CryoSat-2 sea ice thickness data (http://data.ceda.ac.uk/neodc/esacci/sea_ice/data/). The Arctic configuration of the MITgcm is available at https://github.com/oucliangxi/ArcticModel18km_MITGCM website.

References

Ballinger, T. J., J. W. Overland, M. Wang, U. S. Bhatt, E. Hanna, I. Hanssen-Bauer, S.-J. Kim, R. L. Thoman, and J. E. Walsh (2020), Surface air temperature. Arctic Report Card: Update for 2020.

Barnes, E. A., and L. M. Polvani (2015), CMIP5 projections of Arctic Amplification, of the North American/North Atlantic circulation, and of their relationship. *J. Climate.,* **28(13)**, 5254-5271.

Baxter, I., Q. Ding, A. Schweiger, M. L'Heureux, S. Baxter, T. Wang, Q. Zhang, K. Harnos, B. Markle, D. Topal, and J. Lu (2019), How Tropical Pacific Surface Cooling Contributed to Accelerated Sea Ice Melt from 2007 to 2012 as Ice Is Thinned by Anthropogenic Forcing. *J. Climate.,* **32(24)**, 8583-8602.

Bi, H., J. Zhang, Y. Wang, Z. Zhang, Y. Zhang, M. Fu, H. Huang, and X. Xu (2018), Arctic Sea Ice Volume Changes in Terms of Age as Revealed From Satellite Observations. *IEEE J-STARS*, **11**, 2223-2237.

Bi, H., Y. Wang, Y. Liang, W. Sun, X. Liang, Q. Yu, Z. Zhang, and X. Xu (2021), Influences of Summertime Arctic Dipole Atmospheric Circulation on Sea Ice Concentration Variations in the Pacific Sector of the Arctic during Different Pacific Decadal Oscillation Phases. *J. Climate.,* **34(8)**, 3003-3019.

Bushuk, M., M. Winton, D. B. Bonan, E. Blanchard-Wrigglesworth, and T. Delworth (2020), A mechanism for the Arctic sea ice spring predictability barrier. *Geophys. Res. Lett.,* **47**, e2020GL088335. https://doi.org/10.1029/2020GL088335.

Castro-Morales, K., F. Kauker, M. Losch, S. Hendricks, K. Riemann-Campe, and R.

Gerdes (2014), Sensitivity of simulated Arctic sea ice to realistic ice thickness distributions and snow parameterizations, *J. Geophys. Res.,* **119**, doi:10.1002/2013JC009342.

Cohen, J., J. A. Screen, J. C. Furtado, M. Barlow, D. Whittleston, D. Coumou, J. Francis, K. Dethloff, D. Entekhabi, J. Overland, and J. Jones (2017), Recent arctic amplification and extreme mid-latitude weather. *Nat. Geosci.,* **7(9)**, 627-637.

Comiso, J. C., and D. K. Hall (2014), Climate trends in the Arctic as observed from space. *Wires. Clim. Change.,* **5(3)**, 389-409.

Curry, J. A., J. L. Schramm, and E. E. Ebert (1995), Sea ice-albedo climate feedback mechanism. *J. Climate.,* **8**, 240-247.

Ding, Q., A. Schweiger, M. L'Heureux, D. S. Battisti, S. Po-Chedley, N. C. Johnson, E. Blanchard-Wrigglesworth, K. Harnos, Q. Zhang, R. Eastman, and E. J. Steig (2017), Influence of high-latitude atmospheric circulation changes on summertime arctic sea ice. *Nat. Clim. Change.,* **7(4)**, 289-295.

Fetterer, F., K. Knowles, W. N. Meier, M. Savoie, and A. K. Windnagel (2017), Sea Ice Index, Version 3. Boulder, Colorado USA. NSIDC: National Snow and Ice Data Center, doi: https://doi.org/10.7265/N5K072F8.

Flocco, D., D. Schroeder, D. L. Feltham, and E. C. Hunke (2012), Impact of melt ponds on Arctic sea ice simulation from 1990 to 2007, *J. Geophys. Res.,* **117**, C09032, doi:10.1029/2012JC008195.

Francis, J. A., and S. J. Vavrus (2015), Evidence for a wavier jet stream in response to rapid arctic warming. *Environ. Res. Lett.,* **10(1)**, 014005.

Gao, Y., J. Sun, F. Li, S. He, S. Sandven, Q. Yan, Z. Zhang, K. Lohmann, N. Keenlyside, T. Furevik, and L. Suo (2015), Arctic sea ice and Eurasian climate: A review. *Adv. Atmos. Sci.*, **32(1)**, 92-114, doi: 10.1007/s00376-014-0009-6.

Graversen, R. G., T. Mauritsen, S. Drijfhout, M. Tjernstrom, and S. Martensson (2011), Warm winds from the Pacific caused extensive Arctic sea-ice melt in summer 2007. *Clim. Dynam.,* **36**, 2103-2112.

Harada, Y., H. Kamahori, C. Kobayashi, H. Endo, S. Kobayashi, Y. Ota, H. Onoda, K. Onogi, K. Miyaoka, and K. Takahashi (2016), The JRA-55 Reanalysis: Representation of atmospheric circulation and climate variability, *J. Meteor. Soc. Japan.,* **94**, 269-302, doi:10.2151/jmsj.2016-015.

Hendricks, S., S. Paul, E. Rinne (2018), ESA Sea Ice Climate Change Initiative (Sea_Ice_cci): Northern hemisphere sea ice thickness from the CryoSat-2 satellite on a monthly grid (L3C), v2.0. Centre for Environmental Data Analysis, doi:10.5285/ff79d140824f42dd92b204b4f1e9e7c2.

Hendricks, S., S. Paul, E. Rinne (2018), ESA Sea Ice Climate Change Initiative (Sea_Ice_cci): Northern hemisphere sea ice thickness from the Envisat satellite on a monthly grid (L3C), v2.0. Centre for Environmental Data Analysis, doi:10.5285/f4c34f4f0f1d4d0da06d771f6972f180.

Hibler III, W. D. (1979), A dynamic thermodynamic sea ice model, *J. Phys. Oceanogr.,* **9(4)**, 815-846.

Hibler III, W. D. (1980), Modeling a variable thickness sea ice cover, *Mon. Weather.*

Rev., **108(2)**, 1943-1973.

Hibler III, W. D. (1984), The role of sea ice dynamics in modelling CO2 increases, in Climate Processes and Climate Sensitivity, edited by J. E. Hansen, and T. Takahashi, pp. 238-253, AGU, Washington, D. C.

Hovelsrud, G., M. McKenna, and H. Huntington (2008), Marine mammal harvests and other interactions with humans, *Ecol. Appl.,* **18(2)**, 135-147.

Jackson, J. M., E. C. Carmack, F. A. McLaughlin, S. E. Allen, and R. G. Ingram (2010), Identification, characterization, and change of the near-surface temperature maximum in the Canada Basin, 1993-2008, *J. Geophys. Res.,* **115**, C05021, doi:10.1029/2009JC005265.

Kay, J. E., T. L'Ecuyer, A. Gettelman, G. Stephens, and C. O'Dell (2008), The contribution of cloud and radiation anomalies to the 2007 Arctic sea ice extent minimum, *Geophys. Res. Lett.,* **35**, L08503, doi:10.1029/2008GL033451.

Keen, A., E. Blockley, D. A. Bailey, J. Boldingh Debernard, M. Bushuk, S. Delhaye, D. Docquier, D. Feltham, F. Massonnet, S. O'Farrell, L. Ponsoni, J. M. Rodriguez, D. Schroeder, N. Swart, T. Toyoda, H. Tsujino, M. Vancoppenolle, and K. Wyser (2021), An inter-comparison of the mass budget of the Arctic sea ice in CMIP6 models, *Cryosphere.,* **15**, 951-982.

Kobayashi, S., Y. Ota, Y. Harada, A. Ebita, M. Moriya, H. Onoda, K. Onogi, H. Kamahori, C. Kobayashi, H. Endo, K. Miyaoka, and K. Takahashi (2015), The JRA-55 Reanalysis: General specifications and basic characteristics. *J. Meteor. Soc. Japan.*, **93**, 5-48, doi:10.2151/jmsj.2015-001.

Kwok, R. (2007), Near zero replenishment of the Arctic multiyear sea ice cover at the end of 2005 summer, *Geophys. Res. Lett.,* **34**, L05501, doi:10.1029/2006GL028737.

Kwok, R. (2018), Arctic sea ice thickness, volume, and multiyear ice coverage: losses and coupled variability (1958–2018). *Environ. Res. Lett.,* **13**, 105005.

Kwok, R., and D. A. Rothrock (2009), Decline in Arctic sea ice thickness from submarine and ICESat records: 1958 – 2008, *Geophys. Res. Lett.,* **36**, L15501, doi:10.1029/2009GL039035.

L'Heureux, M. L., A. Kumar, G. D. Bell, M. S. Halpert, and R. W. Higgins (2008), Role of the Pacific-North American (PNA) pattern in the 2007 Arctic sea ice decline, *Geophys. Res. Lett.,* **35**, L20701, doi:10.1029/2008GL035205.

Lang, A., S. Yang, and E. Kaas (2017), Sea ice thickness and recent Arctic warming. *Geophys. Res. Lett.,* **44**, 409-418.

Lee, H. J., M. O. Kwon, S.-W. Yeh, Y.-O. Kwon, W. Park, J.-H. Park, Y. H. Kim, and M. A. Alexander (2017), Impact of poleward moisture transport from the North Pacific on the acceleration of sea ice loss in the Arctic since 2002. *J. Climate.,* **30**, 6757-6769.

Liang, X., and M. Losch (2018), On the effects of increased vertical mixing on the Arctic Ocean and sea ice. *J. Geophys. Res. Oceans.,* **123**, 9266-9282.

Liang, X., M. Losch, L. Nerger, L. Mu, Q. Yang, and C. Liu (2019), Using sea surface temperature observations to constrain upper ocean properties in an Arctic sea ice-ocean data assimilation system. *J. Geophys. Res. Oceans.,* **124**, 4727-4743.

Lindsay, R. W., and A. Schweiger (2015), Arctic sea ice thickness loss determined using subsurface, aircraft, and satellite observations. *Cryosphere*, **9**, 269-283.

Lindsay, R. W., and J. Zhang (2005), The thinning of Arctic sea ice, 1988-2003: Have we passed a tipping point? *J. Climate.,* **18(22)**, 4879-4894.

Lindsay, R. W., J. Zhang, A. Schweiger, M. Steele, and H. Stern (2009), Arctic sea ice retreat in 2007 follows thinning trend. *J. Climate.,* **22(1)**, 165-176.

Locarnini, R. A., A. V. Mishonov, J. I. Antonov, T. P. Boyer, and H. E. Garcia (2006), World Ocean Atlas 2005, Volume 1: Temperature. S. Levitus, Ed. NOAA Atlas NESDIS 61, U.S. Government Printing Office, Washington, D.C., 182 pp.

Losch, M., D. Menemenlis, J. M. Campin, P. Heimbach, and C. Hill (2010), On the formulation of sea-ice models. Part 1: Effects of different solver implementations and parameterizations. *Ocean. Model.,* **33**, 129-144.

Lukovich, J. V., J. C. Stroeve, A. Crawford, L. Hamilton, M. Tsamados, H. Heorton, and F. Massonnet (2021), Summer Extreme Cyclone Impacts on Arctic Sea Ice, J. Climate., 34, 4817-4834.

Marshall, J., A. Adcroft, C. Hill, L. Perelman, and C. Heisey (1997), A finite-volume, incompressible Navier Stokes model for studies of the ocean on parallel computers, *J. Geophys. R*es., **102(C3)**, 5753-5766, doi:10.1029/96JC02775.

Maslanik, J., J. Stroeve, C. Fowler, and W. Emery (2011), Distribution and trends in Arctic sea ice age through spring 2011. *Geophys. Res. Lett.,* **38**, L13502, doi:10.1029/2011GL047735.

Meier, W. N., F. Fetterer, M. Savoie, S. Mallory, R. Duerr, and J. Stroeve (2013), NOAA/NSIDC Climate Data Record of Passive Microwave Sea Ice Concentration, Version 2. Boulder, Colorado USA. NSIDC: National Snow and Ice Data Center. doi: https://doi.org/10.7265/N55M63M1.

Meier, W. N., G. K. Hovelsrud, B. E. H. van Oort, J. R. Key, K. M. Kovacs, C. Michel, C. Haas, M. A. Granskog, S. Gerland, D. K. Perovich, A. Makshtas, and J. D. Reist (2014), Arctic sea ice in transformation: A review of recent observed changes and impacts on biology and human activity, *Rev. Geophys.,* **51**, doi:10.1002/2013RG000431.

Menemenlis, D., J. M. Campin, P. Heimbach, C. Hill, T. Lee, A. Nguyen, M. Schodlok, and H. Zhang (2008), ECCO2: High resolution global ocean and sea ice data synthesis, *Mercator Ocean Q. Newsl.,* **31**, 13-21.

Notz, D., and C. M. Bitz (John Wiley & Sons, Chichester, 2017), in Sea Ice (ed. Tomas, D. N.)

Ogi, M., and J. M. Wallace (2012), The role of summer surface wind anomalies in the summer Arctic sea ice extent in 2010 and 2011, *Geophys. Res. Lett.,* **39**, L09704, doi:10.1029/2012GL051330.

Olonscheck, D., T. Mauritsen, and D. Notz (2019), Arctic sea-ice variability is primarily driven by atmospheric temperature fluctuations. *Nat. Geosci.,* **12(6)**, 430-434.

Overland, J. E., J. A. Francis, E. Hanna, and M. Wang (2012), The recent shift in early summer Arctic atmospheric circulation, *Geophys. Res. Lett.,* **39**, L19804, doi:10.1029/2012GL053268.

Pedersen, L. T., G. Dybkjær, S. Eastwood, G. Heygster, N. Ivanova, S. Kern, T. Lavergne, R. Saldo, S. Sandven, A. Sørensen, and R. T. Tonboe (2017), ESA Sea Ice Climate Change Initiative (Sea_Ice_cci): Sea Ice Concentration Climate Data Record from the AMSR-E and AMSR-2 instruments at 25km grid spacing, version 2.1. Centre for Environmental Data Analysis, 05 October 2017.

Perovich, D. K., K. F. Jones, B. Light, H. Eicken, T. Markus, J. Stroeve, and R. Lindsay (2011), Solar partitioning in a changing Arctic sea-ice cover. *Ann. Glaciol.,* **52(57)**, 7.

Perovich, D. K., J. A. Richter-Menge, K. F. Jones, and B. Light (2008), Sunlight, water, and ice: Extreme Arctic sea ice melt during the summer of 2007, *Geophys. Res. Lett.,* **35**, 2008

Rasmussen, R. O. (2011), Megatrends, TemaNord 2011:527, Nordic Council of Ministers, 2011, Copenhagen.

Ricker, R., S. Hendricks, V. Helm, H. Skourup, and M. Davidson (2014), Sensitivity of CryoSat-2 Arctic sea ice freeboard and thickness on radar-waveform interpretation, *Cryosphere,* **8(4)**, 1607-1622, doi:10.5194/tc-8-1607-2014.

Rigor, I. G., and J. M. Wallace (2004), Variations in the age of Arctic sea-ice and summer sea-ice extent. *Geophys. Res. Lett.,* **31(9)**, L09401.

Schulkes, R. M. S. M. (1995), A note on the evolution equations for the area fraction and the thickness of a floating ice cover. *J. Geophys. R*es., **100(C3)**, 5021-5024.

Screen, J. A., I. Simmonds, C. Deser, and R. Tomas (2013), The atmospheric response to three decades of observed Arctic seaice loss. *J. Climate.,* **26**, 1230-1248.

Semtner Jr., A. J. (1976), A model for the thermodynamic growth of sea ice in numerical investigations of climate. *J. Phys. Oceanogr.,* **6**, 379-389.

Serreze, M. C., and R. G. Barry (2011), Processes and impacts of Arctic Amplification. *Global. Planet. Change*., **77(1-2)**, 85-96.

Serreze, M. C., J. A. Maslanik, T. A. Scambos, F. Fetterer, J. Stroeve, K. Knowles, C. Fowler, S. Drobot, R. G. Barry, and T. M. Haran (2003), A record minimum arctic sea ice extent and area in 2002, *Geophys. Res. Lett.,* **30(3)**, 1110, doi:10.1029/2002GL016406.

Shimada, K., T. Kamoshida, M. Itoh, S. Nishino, E. Carmack, F. McLaughlin, S. Zimmermann, and A. Proshutinsky (2006), Pacific Ocean inflow: Influence on catastrophic reduction of sea ice cover in the Arctic Ocean, *Geophys. Res. Lett.,* **33**, L08605, doi:10.1029/2005GL025624.

Simmonds, I., and I. Rudeva (2012), The great Arctic cyclone of August 2012, *Geophys. Res. Lett.,* **39**, L23709, doi:10.1029/2012GL054259.

Spreen, G., L. Kaleschke, and G. Heygster (2008), Sea ice remote sensing using AMSR-e 89-GHz channels. *J. Geophys. Res. Oceans.,* **113**, C02S03, doi: 10.1029/2005JC003384.

Steele, M., J. Morison, W. Ermold, I. Rigor, M. Ortmeyer, and K. Shimada (2004), Circulation of summer Pacific halocline water in the Arctic Ocean, *J. Geophys. Res.,* **109**, C02027, doi:10.1029/2003JC002009.

Stroeve, J. C., M. C. Serreze, M. M. Holland, J. E. Kay, J. Malanik, and A. P. Barrett (2012), The arctic's rapidly shrinking sea ice cover: a research synthesis. *Climatic Change,* **110(3-4)**, p.1005-1027, doi:10.1007/s10584-011-0101-1.

Swart, N. C., J. C. Fyfe, E. Hawkins, J. E. Kay, and A. Jahn (2015), Influence of internal variability on Arctic sea-ice trends. *Nat. Clim. Change.,* **5(2)**, 86-89.

Tietsche, S., D. Notz, J. H. Jungclaus, and J. Marotzke (2011), Recovery mechanisms of Arctic summer sea ice. *Geophys. Res. Lett.,* **38**, L02707.

Wang, J., J. Zhang, E. Watanabe, M. Ikeda, K. Mizobata, J. E. Walsh, X. Bai, and B. Wu (2009), Is the Dipole Anomaly a major driver to record lows in Arctic summer sea ice extent?, *Geophys. Res. Lett.,* **36**, L05706, doi:10.1029/2008GL036706.

Wang, Z., J. Walsh, S. Szymborski, and M. Peng (2020), Rapid Arctic sea ice loss on the synoptic time scale and related atmospheric circulation anomalies. *J. Climate.,* **33(5)**, 1597-1617.

Winton, M. (2011), Do climate models underestimate the sensitivity of Northern Hemisphere sea ice cover?. *J. Climate.,* **24(15)**, 3924-3934.

Woodgate, R. A., T. Weingartner, and R. Lindsay (2010), The 2007 Bering Strait oceanic heat flux and anomalous Arctic sea-ice retreat. *Geophys. Res. Lett.,* **37**, DOI: 10.1029/2009GL041621.

Wu, B., J. Wang, and J. E. Walsh (2005), Dipole anomaly in the Arctic atmosphere and winter Arctic sea ice motion. *J. Climate.,* **19**, 1529-1536.

Yamagami, A., M. Matsueda, and H. L. Tanaka (2017), Extreme arctic cyclone in august 2016. *Atmos. Sci. Lett.,* **18(7)**, 307-314.

Zhang, J., and W. D. Hibler III (1997), On an efficient numerical method for modeling sea ice dynamics, *J. Geophys. Res.,* **102(C4)**, 8691-8702, doi:10.1029/96JC03744.

Zhang, J., R. Lindsay, M. Steele, and A. Schweiger (2008), What drove the dramatic retreat of arctic sea ice during summer 2007?, *Geophys. Res. Lett.,* **35**, L11505, doi:10.1029/2008GL034005.

Zhang, J., R. Lindsay, A. Schweiger, and M. Steele (2013), The impact of an intense summer cyclone on 2012 arctic sea ice retreat. *Geophys. Res. Lett.,* **40(4)**, 720-726.

Zhang, J., and D. A. Rothrock (2003), Modeling global sea ice with a thickness and enthalpy distribution model in generalized curvilinear coordinates. *Mon. Weather. Rev.,* **131(5)**, 845-861.

Figure Captions

Figure 1. Observed September sea ice edge. The red, blue, orange, green, purple and black lines represent the sea ice edge of 2012, 2020, 2019, 2016, 2007 and the 1987-2019 mean, respectively. The sea ice edge of 2020 is derived from the UB AMSR ASI data. Others are derived from the NSIDC passive microwave sea ice concentration climate data record. UB = University of Bremen. AMSR = Advanced Microwave Scanning Radiometer. ASI = ARTIST Sea Ice. NSIDC = National Snow and Ice Data Center.

Figure 2. The AD time series in melting seasons (May-September) from 2000 to 2020. The solid line denotes the AD time series. The dashed line denotes one standard deviation of the AD time series. The AD index is calculated as the time series of the 2nd leading mode from the Empirical Orthogonal Function analysis applied to the monthly mean sea level pressure in the regions north of 60 °N in the JRA55 data. JRA55 = Japanese 55-year Reanalysis.

Figure 3. Evolution of basin mean (a) upper 200-m averaged ocean temperature in ℃ and (b) sea ice concentration in the CTRLRUN run.

Figure 4. (a) Evolution of sea ice extent from 2002 to 2020 in 10^6 km^2. The black solid, red solid and red dashed lines represent the sea ice extent in the CTRLRUN run, the AMSR ESA-CCI and AMSR ASI data, respectively (b) Evolution of monthly

mean sea ice thickness in the cold season from 2002 to 2020 in meters. The black diamond, red square, red “x” and red triangle represent the sea ice thickness in the CTRLRUN run, ENVISAT ESA-CCI, CRYOSAT2 ESA-CCI and CRYOSAT2 SIRAL data, respectively. The red bars represent the observational uncertainty. AMSR = Advanced Microwave Scanning Radiometer. ESA-CCI = European Space Agency-Climate Change Initiative. ASI = ARTIST Sea Ice. SIRAL = AWI Sea Ice Radar Altimetry.

Figure 5. Modeled and observed sea ice concentration on 24 September. (a, d), (b, e), (c, f), (g, i) and (h, j) show the (modeled, observed) sea ice concentration of 2012, 2020, 2019, 2016 and 2007, respectively. The observations are derived from the AMSR sea ice concentration data. AMSR = Advanced Microwave Scanning Radiometer.

Figure 6. Domain of the control region used in sea ice budget analysis. The red lines represent the boundaries of the control region.

Figure 7. Evolution of sea ice (a) area in 10^6 km^2 and (b) volume in 10^3 km^3 in the control region in the CTRLRUN run. The cyan, red, black, green and blue lines represent the growth-decay evolution during 2006-2007, 2011-2012, 2015-2016, 2018-2019 and 2019-2020, respectively.

Figure 8. Daily increments of sea ice (a) area in 10^4 km^2 and (b) volume in km^3 in the control region from September 2011 to September 2012 in the CTRLRUN run. The blue, green, magenta, red, cyan, and black lines in the top panel represent the $<\omega_{io}>$, $<\omega_{ai}>$, $<\omega_{ao}>$, $<\partial\psi_{advx}/\partial x+\partial\psi_{advy}/\partial y>$, $<\omega_{ridging}>$, and ΔA term, respectively. The blue, green, magenta, yellow, red, and black lines in the bottom panel represent the $<\theta_{io}>$, $<\theta_{ai}>$, $<\theta_{ao}>$, $<\theta_{fl}>$, $<\partial\varphi_{advx}/\partial x+\partial\varphi_{advy}/\partial y>$, and ΔV term, respectively.

Figure 9. Accumulated sea ice area increments in 10^6 km^2 from 1 May due to (a) ΔA, (b) $<\omega_{io}>$, (c) $<\omega_{ai}>$, (d) $<\omega_{ao}>$, (e) $<\partial\psi_{advx}/\partial x+\partial\psi_{advy}/\partial y>$, and (f) $<\omega_{ridging}>$ in the control region in the CTRLRUN run. The cyan, red, black, green, and blue lines represent the decay evolution during 2006-2007, 2011-2012, 2015-2016, 2018-2019, and 2019-2020, respectively.

Figure 10. Accumulated sea ice volume increments in 10^3 km^3 from 1 September of the previous year to (a) 1 May and (b) 1 September. The cyan, red, black, green, and blue bars represent the sea ice volume budget terms in 2006-2007, 2011-2012, 2015-2016, 2018-2019 and 2019-2020, respectively. The snow flooding terms are not shown because they are negligible.

Figure 11. Comparison of the modeled sea ice extent evolution from 1 May in 10^6 km^2 in the control region between the baseline and sensitivity runs. The black line denotes the evolution in 2012 in the CTRLRUN run. The blue, green, purple, orange, red,

brown, pink and gray lines represent the evolution in the sensitivity run 01 to 08, respectively.

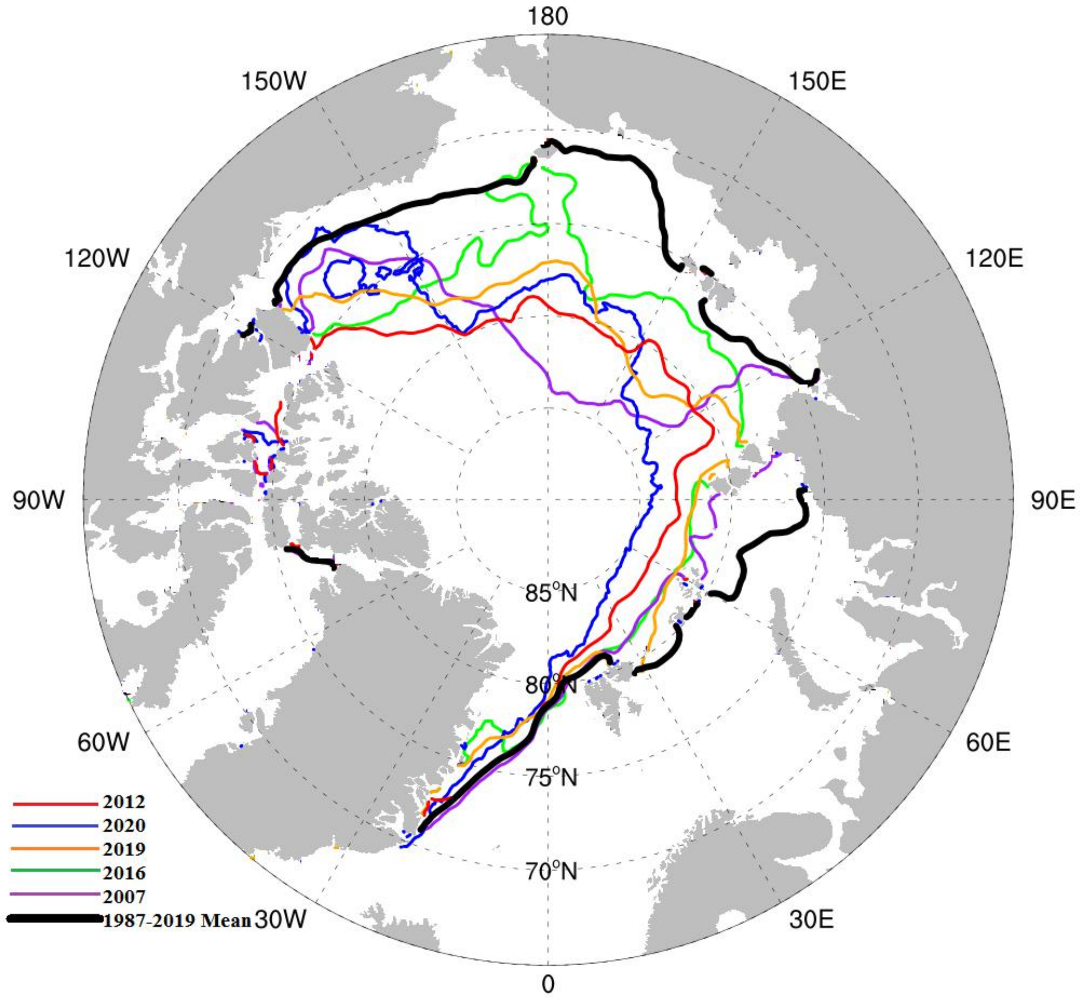

Figure 1. Observed September sea ice edge. The red, blue, orange, green, purple and black lines represent the sea ice edge of 2012, 2020, 2019, 2016, 2007 and the 1987-2019 mean, respectively. The sea ice edge of 2020 is derived from the UB AMSR ASI data. Others are derived from the NSIDC passive microwave sea ice concentration climate data record. UB = University of Bremen. AMSR = Advanced Microwave Scanning Radiometer. ASI = ARTIST Sea Ice. NSIDC = National Snow and Ice Data Center.

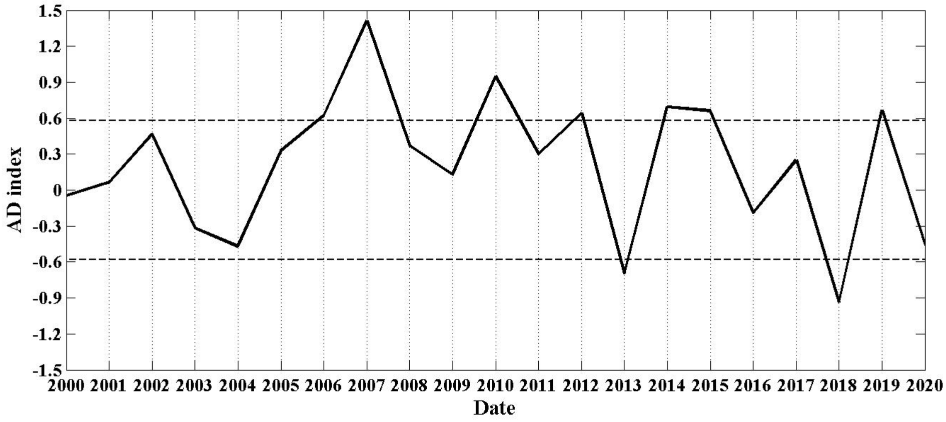

Figure 2. The AD time series in melting seasons (May-September) from 2000 to 2020. The solid line denotes the AD time series. The dashed line denotes one standard deviation of the AD time series. The AD index is calculated as the time series of the 2nd leading mode from the Empirical Orthogonal Function analysis applied to the monthly mean sea level pressure in the regions north of 60 °N in the JRA55 data. JRA55 = Japanese 55-year Reanalysis.

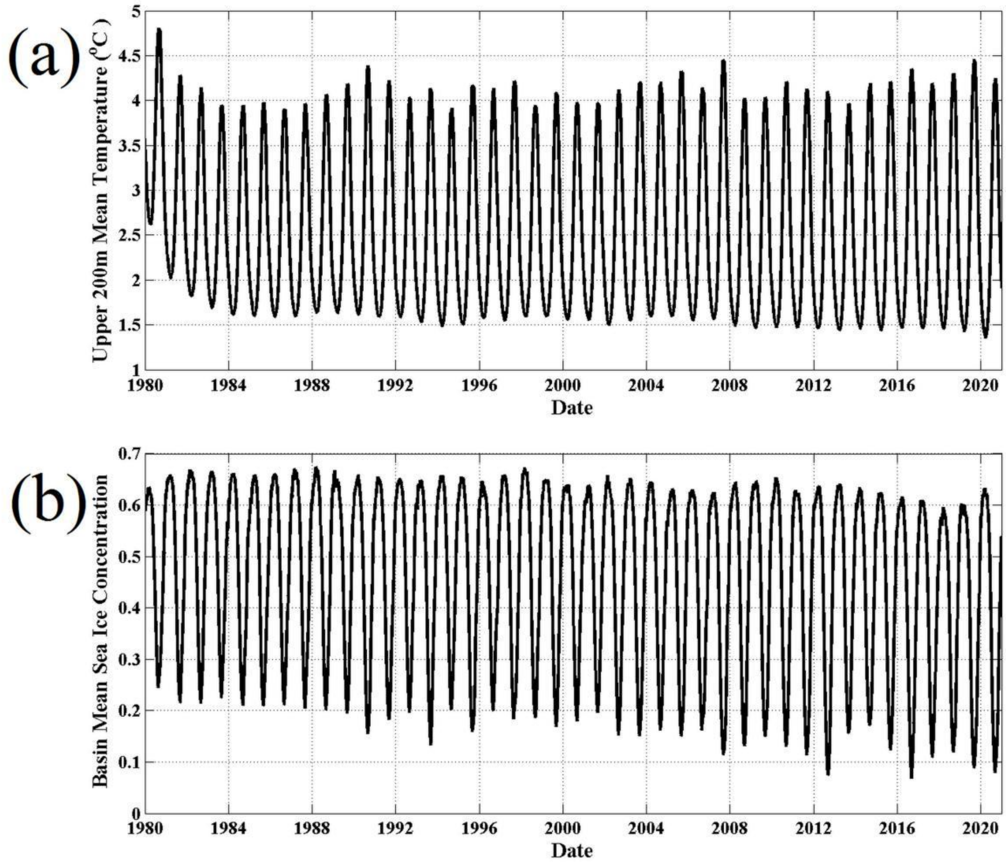

Figure 3. Evolution of basin mean (a) upper 200-m averaged ocean temperature in ℃ and (b) sea ice concentration in the CTRLRUN run.

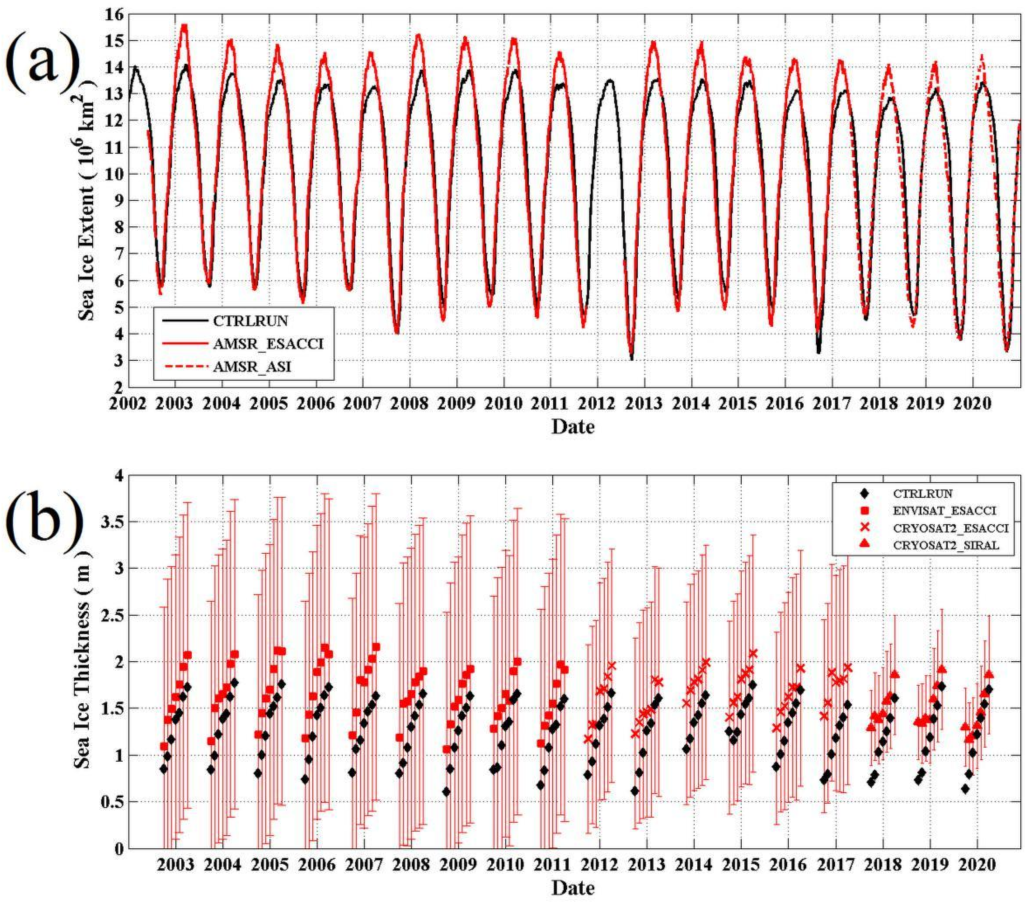

Figure 4. (a) Evolution of sea ice extent from 2002 to 2020 in 10^6 km^2. The black solid, red solid and red dashed lines represent the sea ice extent in the CTRLRUN run, the AMSR ESA-CCI and AMSR ASI data, respectively (b) Evolution of monthly mean sea ice thickness in the cold season from 2002 to 2020 in meters. The black diamond, red square, red "x" and red triangle represent the sea ice thickness in the CTRLRUN run, ENVISAT ESA-CCI, CRYOSAT2 ESA-CCI and CRYOSAT2 SIRAL data, respectively. The red bars represent the observational uncertainty. AMSR = Advanced Microwave Scanning Radiometer. ESA-CCI = European Space Agency-Climate Change Initiative. ASI = ARTIST Sea Ice. SIRAL = AWI Sea Ice Radar Altimetry.

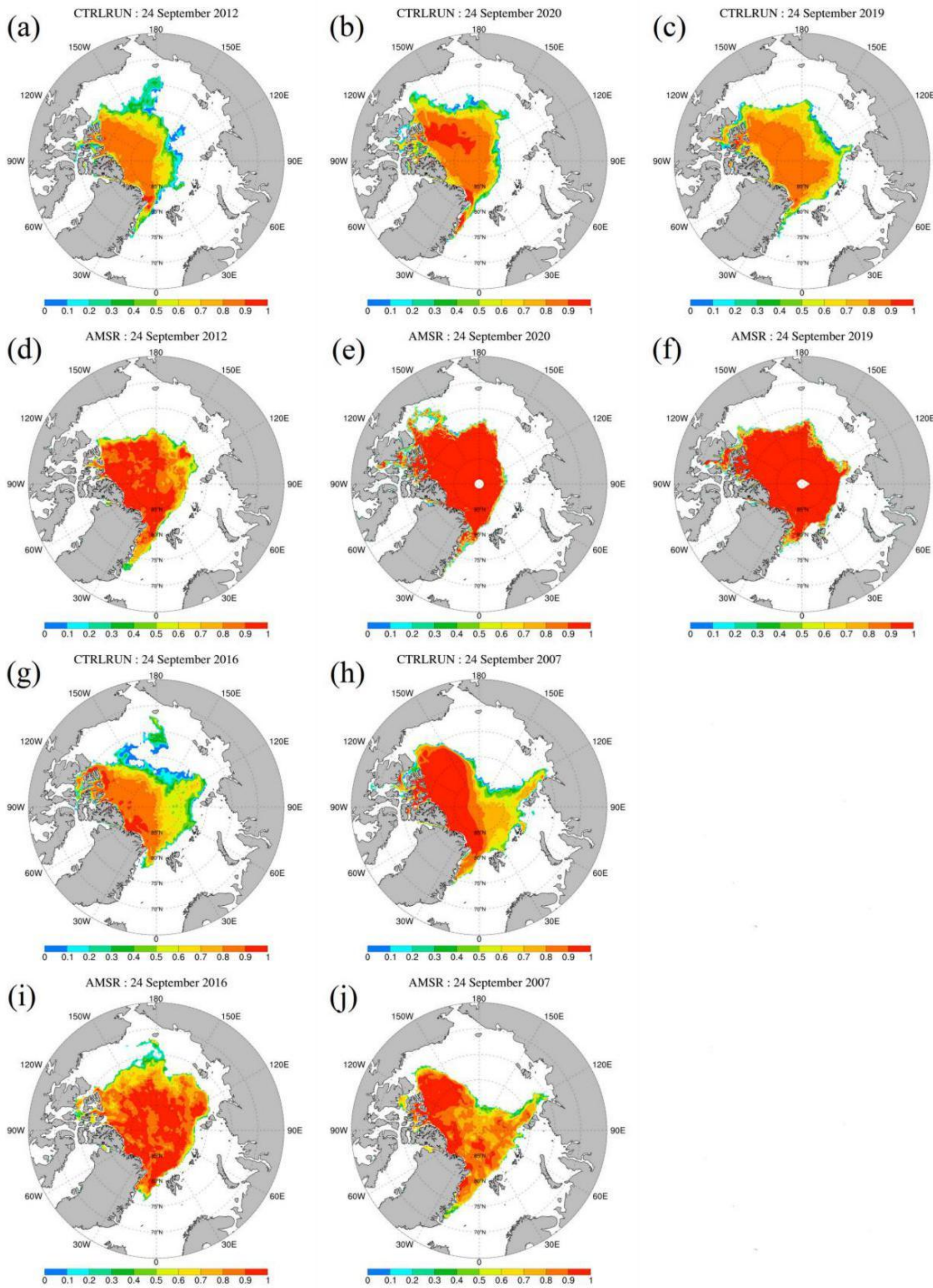

Figure 5. Modeled and observed sea ice concentration on 24 September. (a, d), (b, e), (c, f), (g, i) and (h, j) show the (modeled, observed) sea ice concentration of 2012, 2020, 2019, 2016 and 2007, respectively. The observations are derived from the AMSR sea ice concentration data. AMSR = Advanced Microwave Scanning Radiometer.

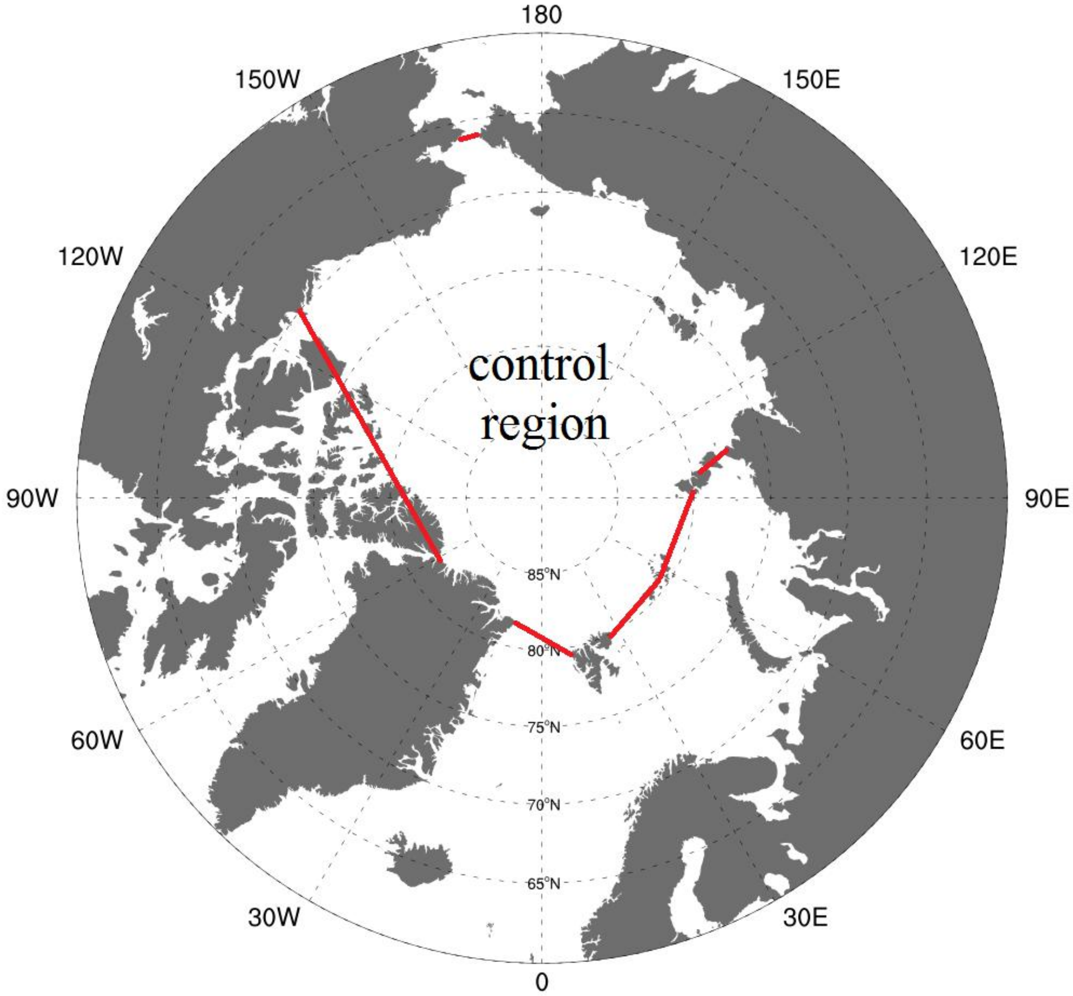

Figure 6. Domain of the control region used in sea ice budget analysis. The red lines represent the boundaries of the control region.

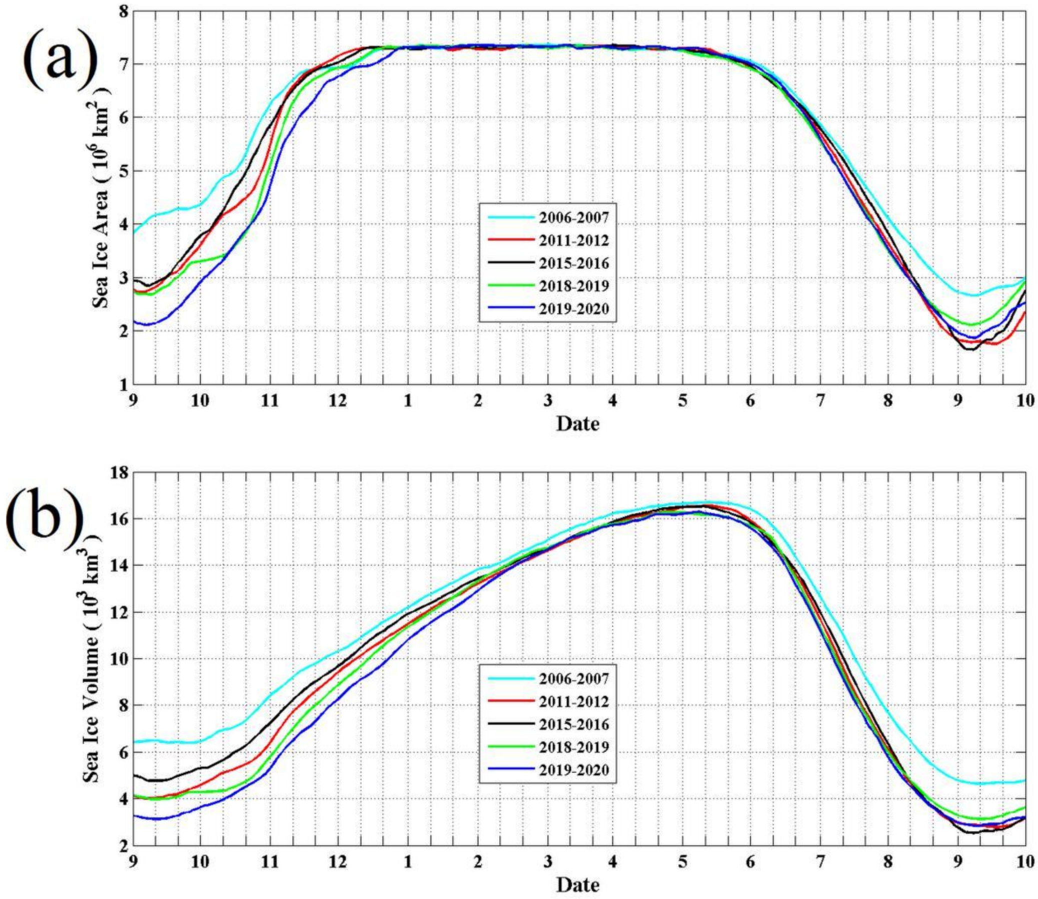

Figure 7. Evolution of sea ice (a) area in 10^6 km^2 and (b) volume in 10^3 km^3 in the control region in the CTRLRUN run. The cyan, red, black, green and blue lines represent the growth-decay evolution during 2006-2007, 2011-2012, 2015-2016, 2018-2019 and 2019-2020, respectively.

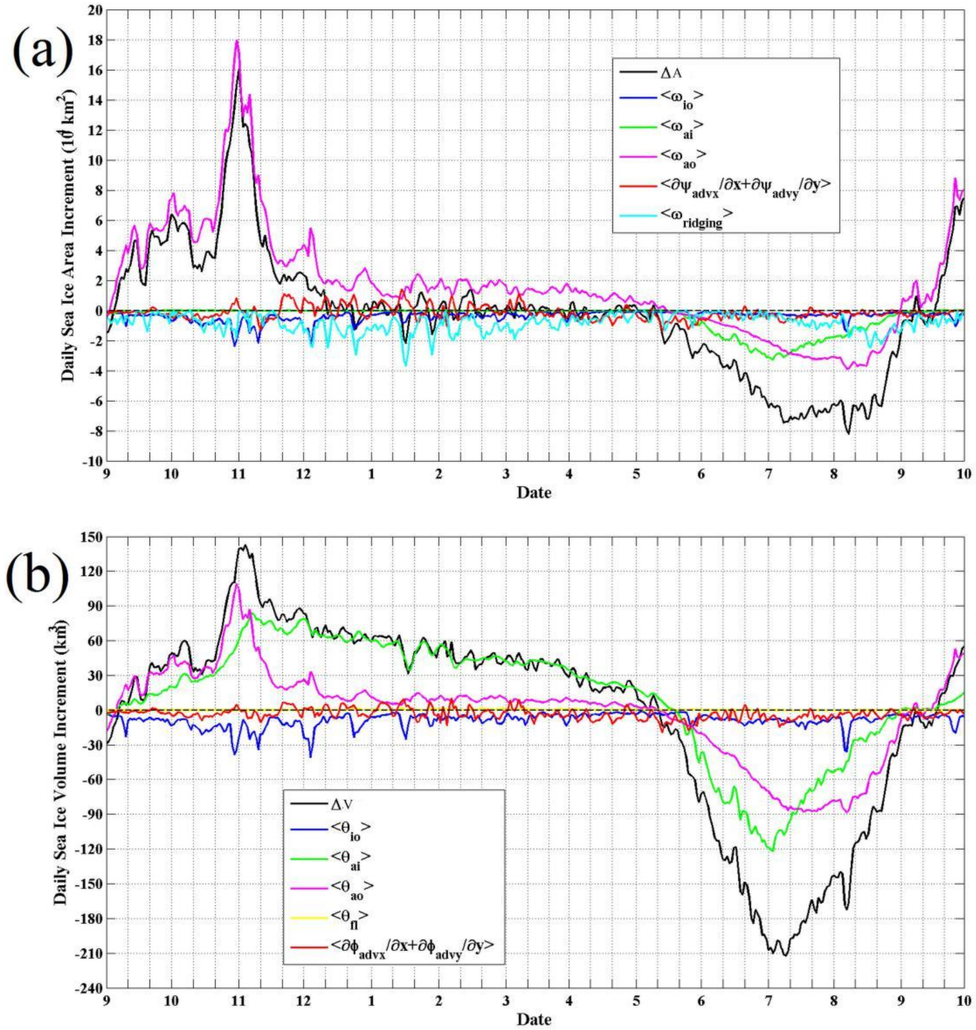

Figure 8. Daily increments of sea ice (a) area in 10^4 km^2 and (b) volume in km^3 in the control region from September 2011 to September 2012 in the CTRLRUN run. The blue, green, magenta, red, cyan, and black lines in the top panel represent the $<\omega_{io}>$, $<\omega_{ai}>$, $<\omega_{ao}>$, $<\partial\psi_{advx}/\partial x+\partial\psi_{advy}/\partial y>$, $<\omega_{ridging}>$, and ΔA term, respectively. The blue, green, magenta, yellow, red, and black lines in the bottom panel represent the $<\theta_{io}>$, $<\theta_{ai}>$, $<\theta_{ao}>$, $<\theta_{fl}>$, $<\partial\varphi_{advx}/\partial x+\partial\varphi_{advy}/\partial y>$, and ΔV term, respectively.

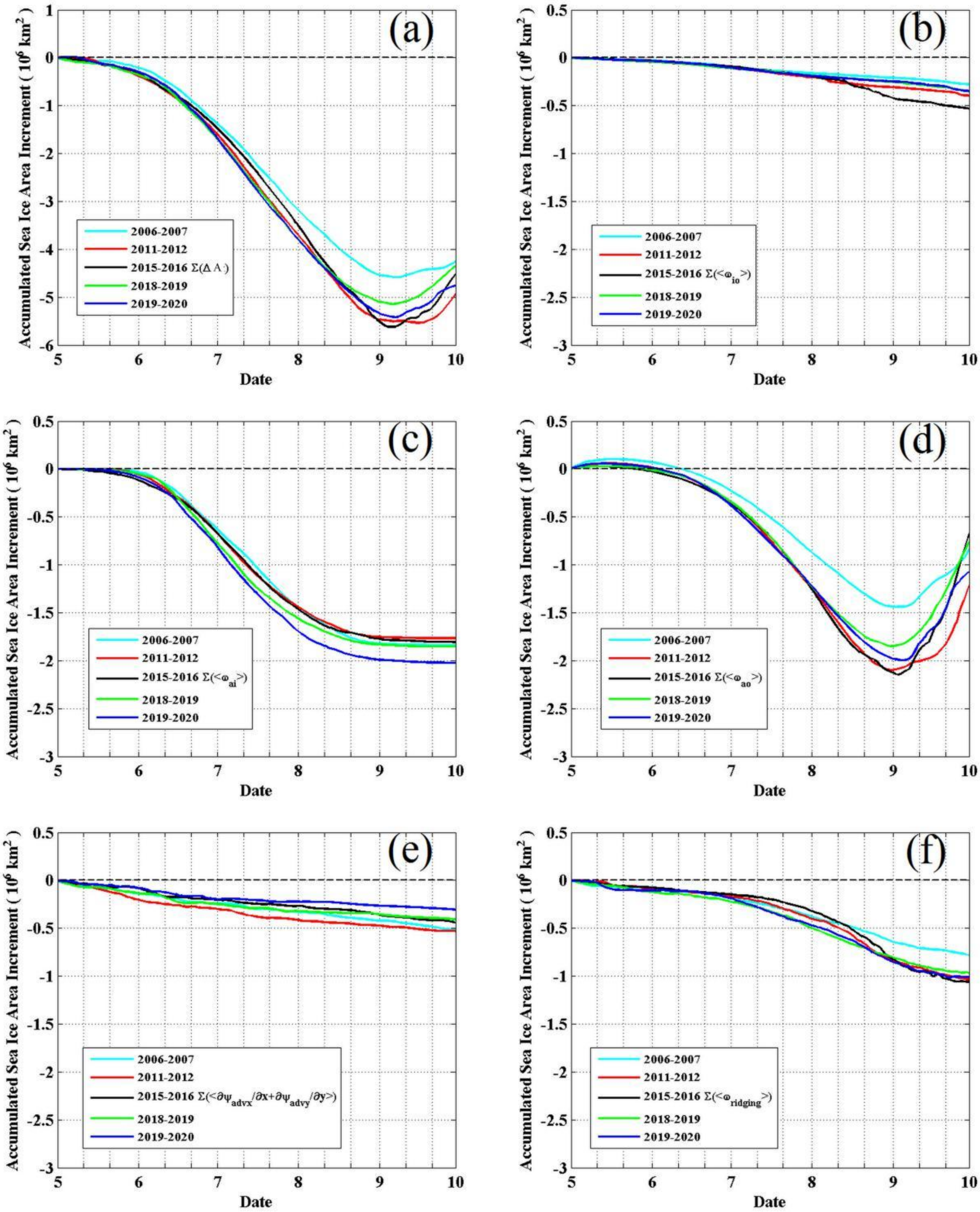

Figure 9. Accumulated sea ice area increments in 10^6 km^2 from 1 May due to (a) ΔA, (b) $<\omega_{io}>$, (c) $<\omega_{ai}>$, (d) $<\omega_{ao}>$, (e) $<\partial\psi_{advx}/\partial x+\partial\psi_{advy}/\partial y>$, and (f) $<\omega_{ridging}>$ in the control region in the CTRLRUN run. The cyan, red, black, green, and blue lines represent the decay evolution during 2006-2007, 2011-2012, 2015-2016, 2018-2019, and 2019-2020, respectively.

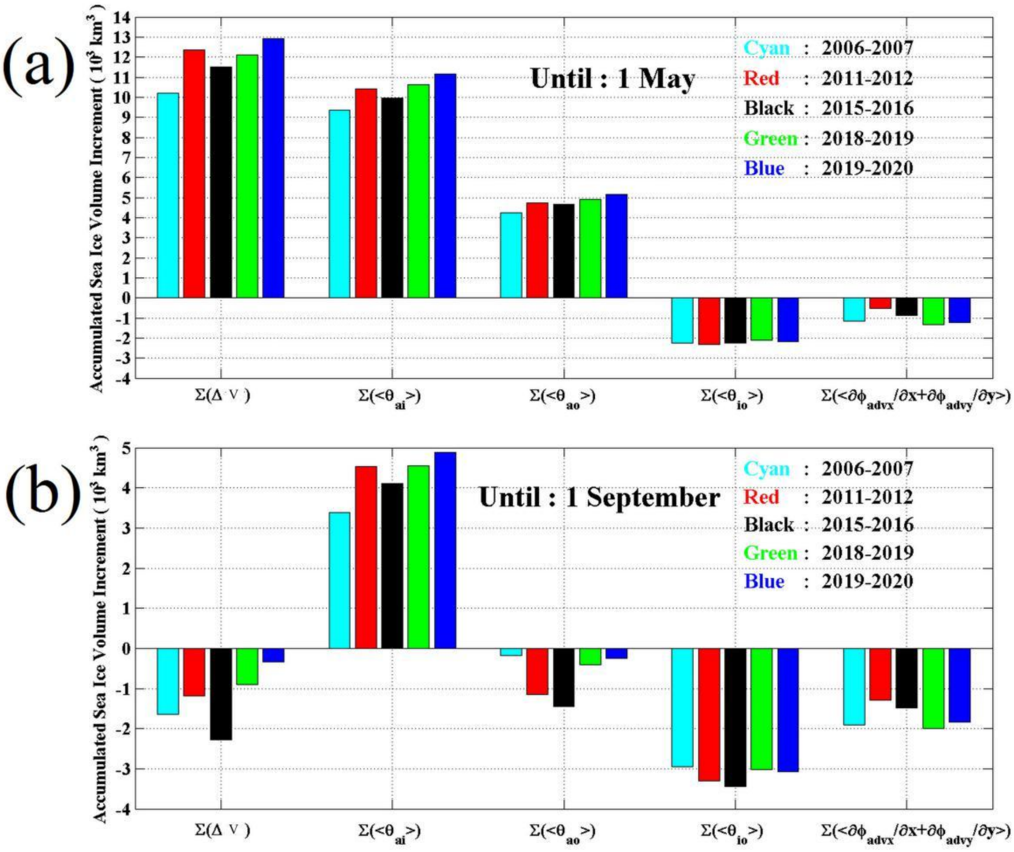

Figure 10. Accumulated sea ice volume increments in 10^3 km^3 from 1 September of the previous year to (a) 1 May and (b) 1 September. The cyan, red, black, green, and blue bars represent the sea ice volume budget terms in 2006-2007, 2011-2012, 2015-2016, 2018-2019 and 2019-2020, respectively. The snow flooding terms are not shown because they are negligible.

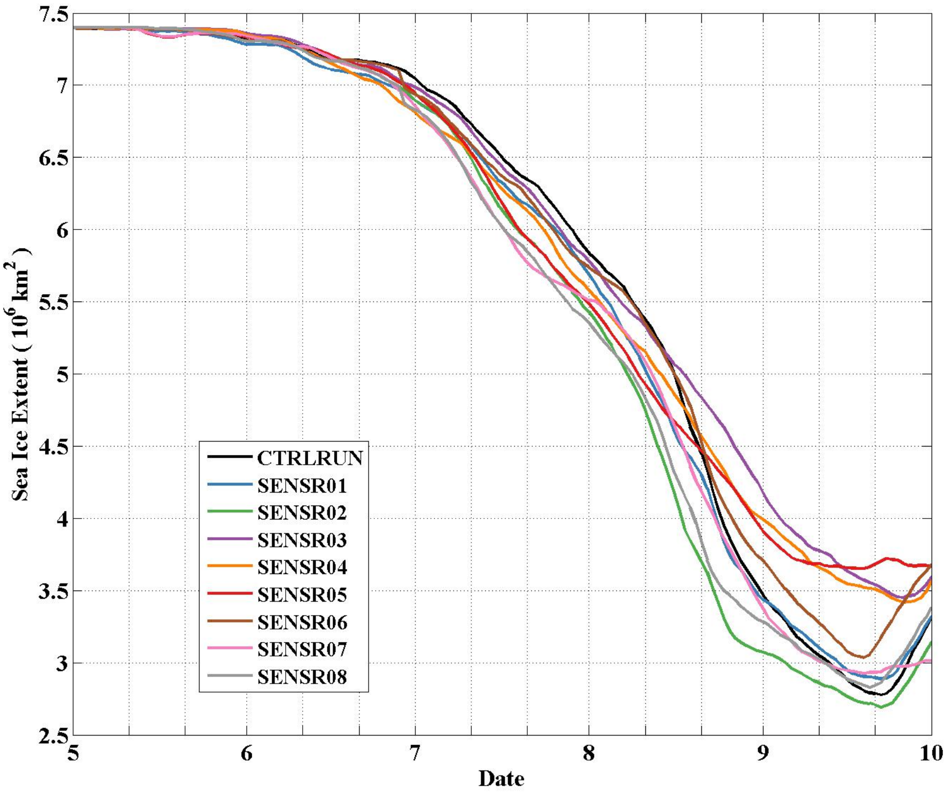

Figure 11. Comparison of the modeled sea ice extent evolution from 1 May in 10^6 km^2 in the control region between the baseline and sensitivity runs. The black line denotes the evolution in 2012 in the CTRLRUN run. The blue, green, purple, orange, red, brown, pink and gray lines represent the evolution in the sensitivity run 01 to 08, respectively.

Table 1. Experiment details. AFMS = Atmospheric Forcing Mean State between 2007 and 2012; RFCS = Restart File Climatological State; RF07 = Restart File on 1 May 2007; RF12 = Restart File on 1 May 2012; RF20 = Restart File on 1 May 2020; JRA55 = Japanese 55-year Reanalysis.

Experiment ID	Data Length	Initial Field	Atmospheric Forcing (3-hourly JRA55 reanalysis) data period
CTRLRUN	41 years	RFCS	1980.01.01-2020.12.31
SENSR01	5 months	RF07	2012.05.01-2012.10.01
SENSR02	5 months	RF20	2012.05.01-2012.10.01
SENSR03	5 months	RF12	2007.05.01-2007.10.01
SENSR04	5 months	RF20	2007.05.01-2007.10.01
SENSR05	5 months	RF12	2020.05.01-2020.10.01
SENSR06	5 months	RF12	2012.05.01-2012.10.01 but data in 1-15 August is replaced by that in AFMS.
SENSR07	5 months	RF20	2020.05.01-2020.10.01 but data in 1-15 August is replaced by that in 2012
SENSR08	5 months	RF20	2012.05.01-2012.10.01 but data in 1-15 August is replaced by that in AFMS.